JCTC Journal of Chemical Theory and Computation

pubs.acs.org/JCTC

Article

Equivalence of Charge Imbalance and External Electric Fields during Free Energy Calculations of Membrane Electroporation

Gari Kasparyan and Jochen S. Hub*

Cite This: J. Chem. Theory Comput. 2023, 19, 2676−2683

Read Online

ACCESS | Metrics & More | Article Recommendations | Supporting Information

ABSTRACT: Electric fields across lipid membranes play important roles in physiology, medicine, and biotechnology, rationalizing the wide interest in modeling transmembrane potentials in molecular dynamics simulations. Transmembrane potentials have been implemented with external electric fields or by imposing charge imbalance between the two water compartments of a stacked double-membrane system. We compare the two methods in the context of membrane electroporation, which involves a large change of membrane structure and capacitance. We show that, given that Ewald electrostatics are defined with tinfoil boundary conditions, the two methods lead to (i) identical potentials of mean force (PMFs) of pore formation and expansion at various potentials, demonstrating that the two methods impose equivalent driving forces for large-scale transitions at membranes, and (ii) to identical polarization of water within thin water wires or open pores, suggesting that the two methods furthermore impose equivalent local electric fields. Without tinfoil boundary conditions, effects from external fields on pore formation are spuriously suppressed or even removed. Together, our study shows that both methods, external fields and charge imbalance, are well suitable for studying large-scale transitions of lipid membranes that involve changes of membrane capacitance. However, using charge imbalance is technically more challenging for maintaining a constant transmembrane potential since it requires updating of the charge imbalance as the membrane capacitance changes.

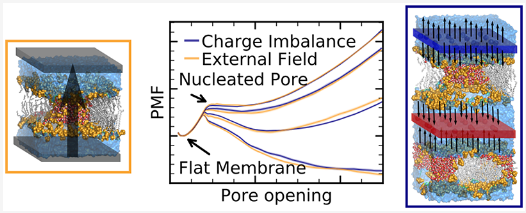

■ INTRODUCTION

Electric fields over lipid membranes play key roles in physiology and biotechnology, explaining the wide interest in modeling transmembrane potentials in molecular dynamics (MD) simulations. Transmembrane potentials have been applied in a plethora of MD studies involving, among others, permeation across ion channels[1−3] or water channels,[4] voltage gating,[5,6] or membrane electroporation.[7−12] These simulations provided unprecedented mechanistic and energetic insight into complex transitions at biological membranes. Membrane electroporation, which is in the focus of the present study, denotes the formation of pores into lipid bilayers by the application of transmembrane electric potentials.[13−15] Reversible electroporation is widely used in biotechnology or medicine to deliver biological samples such as genes, vaccines, or drugs into living cells.[16] Furthermore, irreversible electroporation is used to kill malignant cells for the ablation of tumor tissue that is not accessible to surgery.[17,18]

Two methods have been put forward for implementing transmembrane potentials in MD simulations. First, external electric fields $\mathbf{E}$ have been applied along the membrane normal by applying an additional force $q_i\mathbf{E}$ to the atoms, where q_i denotes the partial charge of atom i.[19−21] With an external electric field with magnitude E_z along the z-axis of the simulation box, the overall potential drop along the box is given by E_zL_z, where L_z is the box dimension along the z direction.[21,22] In the presence of a lipid membrane oriented in the $x-y$ plane, the potential drops mostly over the low-dielectric membrane core, hence imposing a transmembrane potential of $V_m = E_zL_z$. Several studies used external electric fields to drive membrane electroporation.[7,8,10−12,23−26]

Alternatively, transmembrane potentials have been implemented by simulating a system with two stacked membranes, thereby forming two solvent reservoirs.[4,9,12,23,27,28] In this setup, the potential is imposed using a charge imbalance between the reservoirs, i.e., by adding ions with excess charges $+Q$ and $-Q$ into the two solvent reservoirs, respectively. This setup has been referred to as “charge imbalance”, “ion imbalance”, or “double-membrane setup”. The charge imbalance Q required for obtaining a specific transmembrane potential V_m is not obvious since it depends on the capacitance C of the membrane via $Q = CV_m$, while the membrane capacitance depends on the thickness, internal structure, and protein content. Hence, Q is typically modified by trial and error until the observed transmembrane potential agrees with the desired value. Upon structural transitions of the membrane such as the formation of a transmembrane pore, the capacitance may greatly change, suggesting that Q must be

Received: January 14, 2023
Published: April 13, 2023

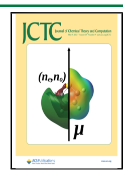

updated for maintaining a constant V_m. An extension of the charge imbalance setup is given by the "computational electrophysiology" method, which maintains a constant transmembrane potential after ion permeation by placing back permeated ions.[29]

Defacto standards of biomolecular MD simulations involve the use of three-dimensional periodic boundary conditions to avoid surface artifacts and the use of Ewald sums[30] for evaluating the long-range electrostatic interactions. Many modern MD codes implement Ewald sums via the computationally efficient particle-mesh Ewald (PME) method.[31,32] Ewald sums are typically evaluated assuming so-called tinfoil boundary conditions, implying that the periodic lattice of unit cells is at a large distance surrounded by a conducting medium. However, the use of Ewald sums with tinfoil boundary conditions together with external fields has been considered as problematic because the external field induces a macroscopic dipole in the simulation box, which seems to be at odds with the assumption of a conducting surrounding medium.[33] Hence, it has been discussed whether the external field may be straightforwardly compared with fields under experimental conditions.[10,11,33,34] In a similar spirit, spurious water ordering effects due to the presence of a macroscopic dipole in simulation systems with an asymmetric lipid membrane have been described recently.[35]

Several studies compared the effects of external electric fields with effects of charge imbalance.[12,23,36] Vernier et al. obtained similar pore formation times when using electric fields or charge imbalance in the presence of large potentials of 1.3 to 2.2 V.[23] Melcr et al. showed that the two methods yield equivalent ion and charge density distributions, water dipole orientations, and local electric fields around a lipid bilayer. However, since Melcr et al. focused on planar membranes, it has not been tested whether the two methods are equivalent during transmembrane pore formation, which involves large changes of membrane capacitance. In addition, it remained unclear whether electric fields implemented with the two methods impose equivalent free energy gradients for conformational transitions that are driven by transmembrane potentials.

Here, we simulated membrane electroporation across a dipalmitoylphosphatidylcholine (DPPC) membrane using either external electric fields or the charge imbalance method. As a highly sensitive test for the effect of electric fields on the membrane, we computed the potential of mean force (PMF) for pore nucleation and expansion at transmembrane potentials between 0 mV and 600 mV using a recently proposed reaction coordinate.[37] To avoid that ions, which we used to impose the charge imbalance, would diffuse across the open pore, we restrained these ions in the two bulk water compartments. As a probe for the local electric fields acting in the simulation, we computed the average water dipole orientation along the pore axis. We find that, given that PME is applied with tinfoil boundary conditions, external electric fields and charge imbalance yield nearly identical PMFs and dipole orientations, suggesting that the two methods are equally suitable for studying large-scale transitions at biomembranes.

■ METHODS

Simulation Setup and Parameters. The simulation system of a single membrane, composed of 200 dipalmitoylphosphatidylcholine (DPPC) lipids and 12000 water molecules, was set up with the MemGen web server.[38] Lipid interactions were described with the force field by Berger et al.,[39] and the SPC water model was applied.[40] The system was equilibrated with the GROMACS simulation software, version 2018.[41] Electrostatic interactions were described with the PME method with tinfoil boundary conditions if not stated otherwise, implying that the periodic simulation system is surrounded by a conducting medium.[31,32] Dispersion interactions and short-range repulsion was described by a Lennard-Jones potential with a cutoff at 1 nm. The temperature was kept at 323 K using velocity-rescaling (τ = 0.1 ps).[42] The pressure was controlled at 1 bar using weak coupling (τ = 5 ps).[40] A time step of 5 fs was applied. The system was equilibrated until the potential energies and box dimensions were fully converged.

Dipole distributions were computed with the Gromacs module gmx h2order from simulations of umbrella windows (see below) of 520 ns, where the first 20 ns were discarded for equilibration. Errors were computed by block averaging using 10 blocks of 50 ns each.

Reaction Coordinate of Pore Formation. PMFs were computed along a recently proposed joint reaction coordinate ξ_p for pore nucleation and pore expansion.[37] During pore nucleation, ξ_p is equivalent to the chain reaction coordinate ξ_{ch} that quantifies the degree of connectivity of a polar transmembrane defect and takes values $\xi_{ch} \in [0,1)$.[43,44] It was previously shown that PMF calculations along ξ_{ch} using umbrella sampling (US) simulations do not suffer from hysteresis problems and yield converged PMFs within moderate simulation times, in the context of both pore formation[44−46] and stalk formation.[47] The coordinate ξ_p used in this study has been defined as[37]

$$\xi_p(\mathbf{r}) = \xi_{ch}(\mathbf{r}) + H_\varepsilon[\xi_{ch}(\mathbf{r}) - \xi_{ch}^s]\frac{R(\mathbf{r}) - R_0}{R_0} \tag{1}$$

where H_ε is a differentiable variant of the Heaviside step function with a switch interval $[-\varepsilon, \varepsilon]$, $R(\mathbf{r})$ is the radius of an established transmembrane pore, R_0 = 0.419 is the approximate radius of a thin water defect, and ξ_{ch}^s is a user-specified parameter that indicates the position of ξ_{ch} of a thin water defect, that is, the region where the transition from the pore nucleation to the pore expansion regime occurs. Hence, for $\xi_{ch} < \xi_{ch}^s - \varepsilon$, the coordinate ξ_p is equivalent to ξ_{ch} and quantifies the connectivity of the transmembrane defect. For $\xi_{ch} > \xi_{ch}^s + \varepsilon$, ξ_p is given by the pore radius $R(\mathbf{r})$ in units of R_0. For more details on the definition of $\xi_{ch}(\mathbf{r})$ and $R(\mathbf{r})$ we refer to previous work.[37,43]

Additional parameters required for defining ξ_p were chosen as follows. The polar atoms contributing to ξ_p were taken as the oxygen atoms of water as well as the four oxygen atoms of the lipid phosphate groups. The switch region between pore nucleation and pore expansion was defined with the parameters ξ_{ch}^s = 0.925 and ε = 0.05. The radius $R(\mathbf{r})$ of the open pore was computed from the number of polar atoms within a horizontal layer centered in the membrane plane with the thickness of 1.2 nm, where the volume per polar atom was taken as 0.02996 nm^3 corresponding to the volume per water molecule. The cylinder used for defining the chain coordinate ξ_{ch} was composed of 28 slices with a thickness of 0.1 nm each and using a cylinder radius of R_{cyl} = 1.2 nm. Critically, during pore nucleation, the radius of the defect is fully controlled by the force field (together with other simulation parameters such as the temperature) and not by the cylinder radius, as the latter is purely used to control the locality of the defect in the

https://doi.org/10.1021/acs.jctc.3c00065
J. Chem. Theory Comput. 2023, 19, 2676−2683

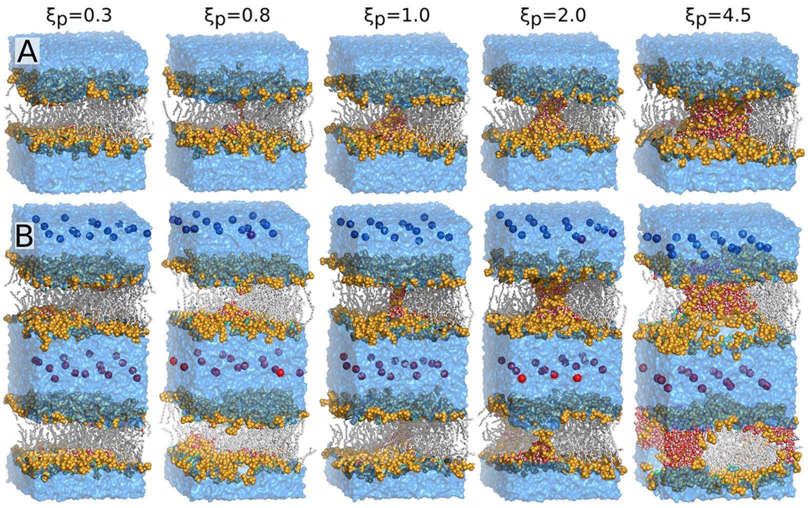

Figure 1. Typical simulation snapshots of pore nucleation and pore expansion, shown (A) for the single-membrane system with external electric field and (B) for the double-membrane system with charge imbalance. Corresponding values of the reaction coordinate ξ_p are shown, which quantifies the degree of connectivity of the transmembrane defect for $\xi_p \lesssim 1$ and the radius R of the pore via $R = \xi_p R_0$ during pore expansion for $\xi_p \gtrsim 1$ (R_0 = 0.419 nm). Headgroup atoms are shown as orange spheres, lipid tails as gray sticks, water in the pore as red/white spheres, and other water as blue surface. Restrained positive and negative dummy charges used to impose the charge imbalance are shown as blue and red spheres, respectively.

membrane plane. The cylinder ensures that two laterally displaced partial defects in the membrane connected with the upper or lower solvent reservoir, respectively, are not misinterpreted as a continuous transmembrane defect, which would lead to hysteresis problems. The length of 2.8 nm of the cylinder was chosen such that approximately 25% of the cylinder slices were filled by polar atoms ($\xi_{ch} \approx 0.25$) in the flat membrane.

Umbrella Sampling Simulations of Pore Formation. Pores were formed by constant-velocity pulling simulations along ξ_p over 100 ns from $\xi_p = 0$ to $\xi_p = 5$ using a force constant of 3000 kJ mol^{-1}. Initial frames for umbrella sampling (US) simulations were taken from the constant-velocity pulling simulation. The PMFs were computed using 52 umbrella windows. Since sampling is more challenging in the switch region between pore nucleation and expansion (i.e., where $\xi_{ch} \approx \xi^s_{ch}$), we used the following nonequidistantly distributed US reference positions and nonequal US force constants: 0.08 to 0.64 in steps of 0.08 (force constant k = 3000 kJ mol^{-1}); 0.69 to 1.03 in steps of 0.02 (k = 5000 kJ mol^{-1}); and 1.18 to 4.93 in steps of 0.15 (k = 400 kJ mol^{-1}). Each window was simulated for 100 ns, and the first 40 ns were removed for equilibration. Statistical errors were estimated using 50 rounds of the Bayesian bootstrap of complete histograms.[48] Statistical errors were in range of few kilojoules per mole (see below).

Charge Imbalance (CI) Simulations. For the CI simulations, a pre-equilibrated simulation system of 200 DPPC lipids (see above) was doubled along the z direction (membrane normal) with the GROMACS module gmx genconf. A grid of 4 × 4 dummy charges was placed at the center of each of the two solvent compartments (Figure 1B, blue and red spheres). The positions of the dummy charges were restrained with harmonic potentials with force constant 10 kJ mol^{-1} nm^{-2}. Hence, the spatial distribution of the charge imbalance in our simulations differed as compared to setups with freely moving ions. However, because the transmembrane potential drops mostly over the membrane and hardly within the water compartment (see below), this difference has only a minor effect. The Lennard-Jones parameters of the dummy charges were taken from the potassium ion of the GROMOS force field[49] as C_6 = 1.63787 × 10^{-5} kJ mol^{-1} nm^6 and C_{12} = 1.18384 × 10^{-6} kJ mol^{-1} nm^{12}.

In order to define dummy charges that yield a desired transmembrane potential, a series of equilibrium simulations was carried out: 20 ns with dummy atoms with charge set to 0e and another 20 ns using charges of 0.1e, where e denotes the unit charge. The resulting transmembrane potential was computed using the gmx potential module, which derives the electrostatic potential profile $\phi(z)$ via a double integration of the one-dimensional Poisson equation. Here, the potential was taken as the difference between the two flat segments of $\phi(z)$ corresponding to the two water regions. According to these simulations, we found that, for an intact membrane, the imposed transmembrane potential followed approximately $V_m = Q/C_{flat}$, where Q is the total absolute charge of each of the charge grids, and the inverse capacitance of the flat membrane was C^{-1}_{flat} = 5.7 V/e with the unit charge e. From this analysis, the initial charges used during US simulations of pore opening were set to $q_{grid} = \pm V_m C_{flat} / n_{grid}$, where n_{grid} is the number of dummy charges per grid.

Iterative Optimization of Charge Imbalance over Rounds of Umbrella Sampling. The capacitance C of the membrane increases with increasing pore radius, suggesting that the charge imbalance Q must be increased in order to maintain a constant transmembrane potential $V_m = Q/C$. We optimized the charge imbalance Q for each umbrella window in an iterative manner. After each round of US, we computed the transmembrane potential and updated Q to obtain increasingly better agreement with the target potential. To reduce the effects of statistical fluctuations, we smoothed the computed potentials along neighboring umbrella windows using a moving average with a window size of three. If the smoothed potential for an umbrella window V^{av}_m differed from the target potential V^t_m by more than 10%, we scaled the charges by V^t_m/V^{av}_m. If the relative deviation was smaller than 10%, we considered the charges as converged.

https://doi.org/10.1021/acs.jctc.3c00065
J. Chem. Theory Comput. 2023, 19, 2676−2683

■ RESULTS AND DISCUSSION

Figure 1 presents typical simulation frames along the pore nucleation and pore expansion pathway, taken from final frames of US windows. Frames are shown for the single-membrane system subject to an external electric field (Figure 1A) and for the double-membrane system subject to a charge imbalance between the two water compartments (Figure 1B). Pore nucleation proceeds from the flat membrane ($\xi_p = 0.25$) via thinning of the membrane involving the protrusion of a polar defect into the membrane core ($\xi_p = 0.85$), the formation of a highly transient water needle, up to the formation of a membrane-spanning polar defect ($\xi_p = 1$). As the pore forms, lipids reorient along the pore rim to partly shield the hydrophobic membrane core from the aqueous defect, as visible from the lipid head groups along the pore rim (Figures 1A,B, right panels). Hence, lipid and water conformations observed during US simulations agree with previous simulations of pore formation.[7,8,23,45,50−54]

Maintaining a Constant Transmembrane Potential in the Double-Membrane Systems Requires Updating of the Charge Imbalance. Figure 2A shows typical potential profiles $\Delta V(z)$ for the double membrane system for transmembrane potentials V_m between 0 mV and 600 mV, here taken from an US simulation with a pore of radius ∼ 1.25 nm ($\xi_p = 3$). The two flat regions at $|z| \approx 9$ nm and $|z| \approx 0$ nm correspond to the two solvent reservoirs that embed the dummy charge layers used to impose the potential. The potential largely drops over the hydrophobic cores of two membranes (3 nm < $|z|$ < 6 nm), as expected due to the lower dielectric permittivity of the membrane cores as compared to the permittivity of the water compartments. The transmembrane potential V_m imposed by the dummy charges is given by the potential difference between the two solvent reservoirs.

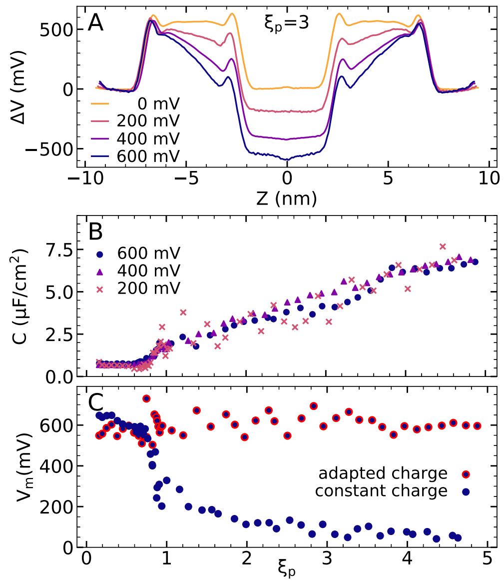

Figure 2. (A) Electrostatic potential profiles $\Delta V(z)$ along the membrane normal z in double membrane systems with potentials of 0 mV, 200 mV, 400 mV, and 600 mV (see legend). (B) Capacitance C of the membrane versus the reaction coordinate of pore formation and pore expansion ξ_p, computed from the transmembrane potential V_m and the charge imbalance Q via $C = Q/V_m$. Symbols (see legend) correspond to values computed from individual US windows. (C) Transmembrane potential obtained from the $\Delta V(z)$ profiles (cf. panel A) with a target potential 600 mV, computed from US windows of various ξ_p values after adapting the charge imbalance for maintaining a constant V_m (red circles) or using a constant charge imbalance (blue circles).

As the pore expands, the capacitance of the membrane increases because part of the low-dielectric membrane core is replaced with high-dielectric water (Figure 2B). Consequently, in the double-membrane system, using a constant charge imbalance would lead to a drop of V_m (Figure 2C, blue circles). To maintain a constant, preselected potential V_m during pore expansion requires updating of the dummy charges. We found that V_m converges slowly within individual US windows, possibly owing to slow rearrangements of the pore shape and of the lipid headgroup structure along the pore rim on the time scale of several tens of nanoseconds. The slow convergence of V_m complicates the identification of the correct charge imbalance that leads to a preselected V_m. Nevertheless, using an iterative procedure, we identified charge imbalances that kept the V_m reasonably constant over all US windows, as shown in Figure 2C (red circles) for simulations with 600 mV.

PMFs of Electroporation Agree between Charge Imbalance and External Field Simulations. We computed the PMFs of pore nucleation and pore expansion using either the double-membrane system (Figure 3, blue lines) or using external electric fields (Figure 3, orange lines). For the double-membrane system, two pores were formed simultaneously in the two membranes (Figure 1B), and the US histograms from the two pore opening processes were combined into a single PMF, thereby providing the free energy per pore. In the PMFs shown in Figure 3, the local minima at $\xi_p \approx 0.25$ corresponding to the flat membrane were taken as a reference point where the free energy was set to zero. The $0.25 \leq \xi_p \lesssim 0.9$ range of the PMFs describes the nucleation of pores, whereas the $\xi_p \gtrsim 1$ region describes the expansion of fully formed polar defects with radii of approximately $R = \xi_p R_0$ with $R_0 = 0.419$ nm. In qualitative agreement with previous simulations of spontaneous pore formation under non-equilibrium conditions[7,8,45,50−54] and with theories of electroporation,[55] application of electric fields leads to a large stabilization of the pore in a voltage- and radius-dependent manner. The physical implications of the PMFs will be

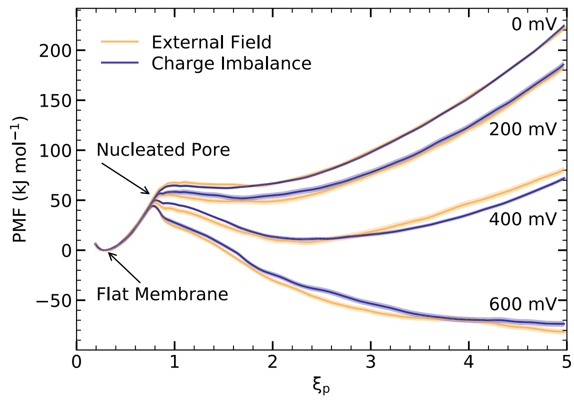

Figure 3. PMF of pore formation over a DPPC membrane involving pore nucleation ($0 < \xi_p \lesssim 0.9$) and pore expansion ($\xi_p \gtrsim 1$) for potentials between 0 mV and 600 mV (see labels) using external electric fields (orange) or charge imbalance (blue). Shaded areas (hardly visible) show standard errors obtained by bootstrapping.

https://doi.org/10.1021/acs.jctc.3c00065
J. Chem. Theory Comput. 2023, 19, 2676−2683

discussed elsewhere.[56] As a key finding of this study, Figure 3 demonstrates that the PMFs based on charge imbalance reveal excellent agreement with the PMFs based on external electric fields. Considering that the PMFs are highly sensitive to modulations of V_m, this agreement suggests that the two methods impose similar electrostatic environments, even during large-scale conformational transitions of membranes as studied here.

Analysis of Water Dipoles Suggests Identical Electric Fields in Charge Imbalance and External Field Simulations. As a probe for the local electric fields along the defect, we computed the average z component of water dipoles $\langle \mu_z^{H_2O} \rangle$ as a function of the z coordinate. In contrast to a similar analysis presented by Melcr et al.[36] who studied the water dipoles for an intact planar membrane, we here computed the dipoles for different degrees of pore opening by averaging within various US simulations. Figure 4 presents

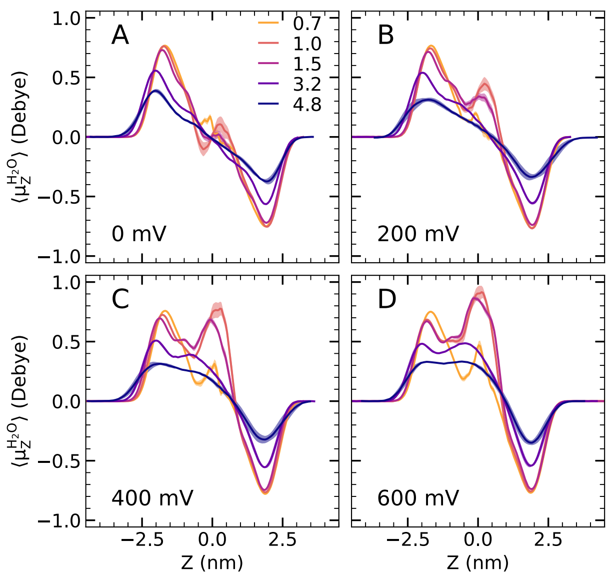

Figure 4. Average dipole per water molecule projected onto the z axis (membrane normal) for (A) 0 mV, (B) 200 mV, (C) 400 mV, and (D) 600 mV for increasing degrees of pore opening, as given by the ξ_p reaction coordinate at 0.7, 1.0, 1.5, 3.2, and 4.8 colored in shades from yellow to blue (see legend). Shaded areas show one standard error. Data was taken from 500 ns simulations with external electric field.

the $\langle \mu_z^{H_2O} \rangle$ profiles with external electric fields taken from US windows with a thinned membrane (ξ_p = 0.7, yellow), with a thin defect with a radius of ~0.42 nm (ξ_p = 1, orange), or with increasingly larger pores (ξ_p = 1.4, red; ξ_p = 3.2, purple; ξ_p = 4.8, blue). At the headgroup regions (|z| ≈ 2 nm), the profiles reveal preferred orientations of water dipoles that diminish with increasing pore opening. At the membrane center (|z| ≈ 0 nm), water in thin transmembrane defects is strongly polarized (Figure 4B−D, ξ_p = 1 or ξ_p = 1.4, orange or red), rationalized by the fact that the membrane-crossing electric field lines concentrate within the higher dielectric. As the pore expands, the electric field decreases inside the pore, leading to decreasingly oriented water dipoles (Figure 4B−D, $\xi_p \geq 3.2$, purple or blue).

To test whether the local electric fields inside the pores agree between the double-membrane and the external field simulations, we compared $\langle \mu_z^{H_2O} \rangle$ obtained from the two simulation setups. Figure 5 presents the profiles for systems

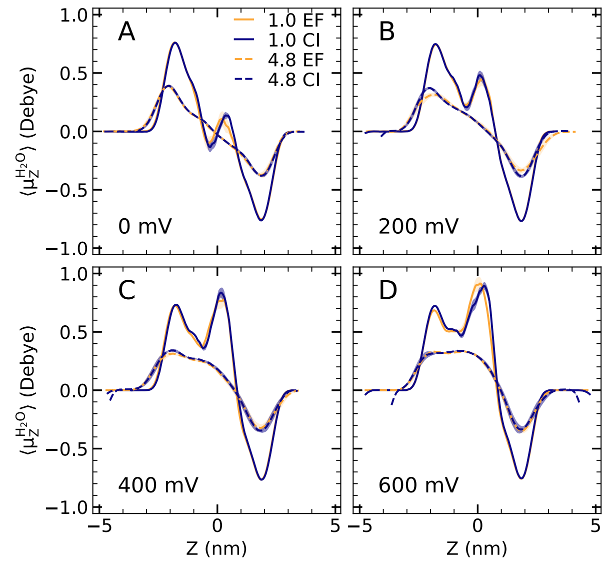

Figure 5. Profiles of average water dipoles, projected onto the z axis, for (A) 0 mV, (B) 200 mV, (C) 400 mV, and (D) 600 mV, using the double-membrane system with charge imbalance (CI, blue) or the external electric field (EF, yellow). Profiles are shown for a thin defect (ξ_p = 1, solid lines) and for a wide open pore (ξ_p = 4.8, dashed lines). Excellent agreement between CI and EF simulations is found. Shaded areas show one standard error. Data was taken from 500 ns simulations.

with a thin pore with a radius of ~0.42 nm (ξ_p = 1, solid lines) or with a wide open pore of radius ~2 nm (ξ_p = 4.8, dashed lines). For systems with identical V_m and identical degree of pore opening, we find excellent agreement between the charge imbalance (Figure 5, yellow lines) and the external field systems (Figure 5, blue lines). These data corroborate the conclusions from the PMFs that charge imbalance and external fields yield highly similar electrostatic environments across the membrane at different degrees of pore opening.

Realistic External Field Simulations Require Tinfoil Boundary Conditions. According to the Ewald formula, the electrostatic energy per simulation unit cell can be decomposed into four contributions: the real space energy, the reciprocal space energy, the self-energy, and a dipole correction.[57,58] The formula assumes that the periodic lattice of unit cells is at a large distance surrounded by a spherical boundary to a surrounding medium with dielectric permittivity ε'. The dipole correction is[57,58]

$$E^{(d)} = \frac{2\pi}{(1 + 2\varepsilon')V_{box}}\mathbf{P}^2 \tag{2}$$

where $\mathbf{P} = \sum_i q_i \mathbf{r}_i$ is the macroscopic dipole of the system with atomic charges q_i and positions $\mathbf{r}_i$, while V_{box} is the box volume. Biomolecular simulations are typically carried out with tinfoil boundary conditions ($\varepsilon' = \infty$) leading to a vanishing dipole correction. With finite ε', in contrast, the dipole correction suppresses the formation of a macroscopic dipole.

To test the effect of the dipole correction during simulations with an external field, we repeated the PMF calculation of pore formation with ε' = 1 or ε' = 80, thereby modeling a surrounding vacuum or a surrounding aqueous medium, respectively (Figure 6). In these simulations, we applied the external field that, with tinfoil boundary conditions, successfully modeled a transmembrane potential of 600 mV (cf. Figure 3). According to the PMFs, using ε' = 80 instead of ε' =

https://doi.org/10.1021/acs.jctc.3c00065
J. Chem. Theory Comput. 2023, 19, 2676−2683

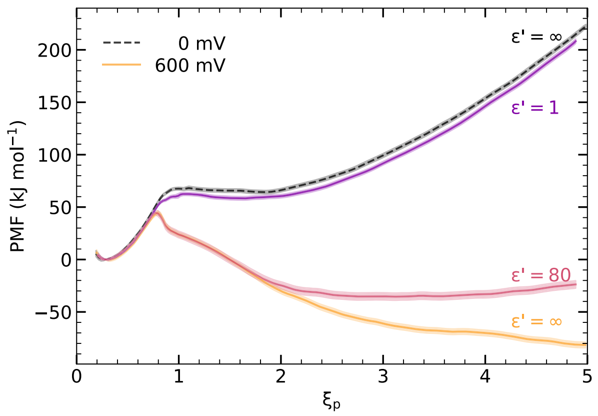

Figure 6. On the importance of using tinfoil boundary conditions: PMFs of pore formation using an external field of 0 mV (black dashed line) or 600 mV (yellow solid line) using PME with tinfoil boundary conditions ($\varepsilon' = \infty$). Red and purple lines: PMFs with the same external electric field as used for the 600 mV simulation but using nonconducting boundary conditions with permittivities $\varepsilon' = 1$ (purple) or $\varepsilon' = 80$ (red).

∞ reduced the effect of the external field on the free energy of a large pore by ~50 kJ/mol (Figure 6, compare red and orange curves). Using $\varepsilon' = 1$, the PMF with an external field (Figure 6, purple) is nearly identical to the PMF computed without external field (Figure 6, black), demonstrating that vacuum boundary conditions suppress the pore-stabilizing effect by the external electric field nearly completely.

The consequence of using vacuum boundary conditions instead of tinfoil boundary conditions is further illustrated from the distributions of water dipoles along open pores (Figure S1). We find that external fields with vacuum boundary conditions ($\varepsilon' = 1$) yield a dipole distribution that is symmetric with respect to the membrane center as requested for a nearly vanishing macroscopic dipole **P**, similar to the case without electric field. Consequently, neither the water in bulk nor the water in the pore are polarized, in sharp contrast to simulations with tinfoil boundary conditions. These data corroborate the observation from the PMFs that nontinfoil boundary conditions suppress or even nearly remove effects from external electric fields. Hence, physically realistic simulations with external fields strictly require tinfoil boundary conditions.

■ CONCLUSIONS

The free energy landscape of membrane pore formation is highly sensitive with respect to transmembrane potentials, as evident from the modulations of pore free energies by tens to hundreds of kilojoules per mole by moderate potentials in the hundreds of millivolt range (Figure 3). Hence, the equivalence of the PMFs obtained either with external electric fields or with charge imbalance suggests that the two methods impose equivalent electrostatic environments on the membrane. We believe that free energy calculations are a rigorous approach for excluding or for quantifying simulation artifacts. Free energy calculations may reveal moderate changes of thermodynamic driving forces which may not be apparent from the analysis of simulation structures alone. An example for such an artifact would be the free energy change of the open pore upon replacing tinfoil boundary conditions (Figure 6, yellow, $\varepsilon' = \infty$) with water boundary conditions (Figure 6, red, $\varepsilon' = 80$); this artifact may not be detected by merely observing pore formation, the pore structures, or dipole orientations (see Figure S1). In a similar spirit, artifacts in non-neutral simulation systems with PME electrostatics have been quantified with free energy calculations[59] and may be corrected during free energy calculations of ligated binding.[60]

Our simulations together with previous results[12,22,23,36] suggest that both external electric fields and charge imbalance provide valid and useful setups for simulating transmembrane potentials, given that tinfoil boundary conditions are applied. However, upon simulating constant potentials in the presence of conformational transitions that modulate the membrane capacitance, the charge imbalance method is technically more challenging since it requires updating of the charges. Since changes of membrane capacitance may only be estimated by geometric considerations, while updating of the charges may induce further alterations of membrane structure and capacitance, an iterative scheme for updating the charges may be required to reach a preselected potential. In contrast, imposing a preselected potential V_m with external electric fields is simple since the external field E_z is related to the transmembrane potentials via $V_m = E_z L_z$, where L_z is the box length in the direction of the electric field.

Membrane electroporation has been simulated extensively under nonequilibrium conditions by applying large transmembrane potentials of several volts.[7,8,10−12,23−25] However, the free energy landscape of pore formation was not well understood, mainly because defining a reaction coordinate of pore formation that enables PMF calculations without hysteresis problems was challenging until recently.[43,44,53] Such understanding will be critical for predicting the influence of different transmembrane potentials or of the lipid and protein content on the kinetics of pore opening and closure and, thereby, on the design of electric field pulse sequences with desired effects on cellular membranes. We anticipate that the present study lays the groundwork for deriving quantitative understanding of electroporation.

■ ASSOCIATED CONTENT

Supporting Information

The Supporting Information is available free of charge at https://pubs.acs.org/doi/10.1021/acs.jctc.3c00065.

Figure S1, analyzing the effect of PME boundary conditions on water dipole orientation (PDF)

■ AUTHOR INFORMATION

Corresponding Author

Jochen S. Hub − *Theoretical Physics and Center for Biophysics, Saarland University, 66123 Saarbrücken, Germany*; orcid.org/0000-0001-7716-1767; Phone: +49 (0)681 302-2740; Email: jochen.hub@uni-saarland.de; Fax: +49 (0)681 302-6604

Author

Gari Kasparyan − *Theoretical Physics and Center for Biophysics, Saarland University, 66123 Saarbrücken, Germany*; orcid.org/0000-0001-6852-8512

Complete contact information is available at: https://pubs.acs.org/10.1021/acs.jctc.3c00065

Notes

The authors declare no competing financial interest.

https://doi.org/10.1021/acs.jctc.3c00065
J. Chem. Theory Comput. 2023, 19, 2676−2683

■ ACKNOWLEDGMENTS

We thank Bert de Groot for insightful discussions. This study was supported by Deutsche Forschungsgemeinschaft (DFG, German Research Foundation; Grants SFB 803/A12, SFB 1027/B7, and INST 256/539-1).

■ REFERENCES

(1) Allen, T. W.; Andersen, O. S.; Roux, B. Energetics of Ion Conduction through the Gramicidin Channel. *Proc. Natl. Acad. Sci. U.S.A.* **2004**, *101*, 117−122.
(2) KÖpfer, D. A.; Song, C.; Gruene, T.; Sheldrick, G. M.; Zachariae, U.; de Groot, B. L. Ion Permeation in K^+ Channels Occurs by Direct Coulomb Knock-On. *Science* **2014**, *346*, 352−355.
(3) Aksimentiev, A.; Schulten, K. Imaging α-Hemolysin with Molecular Dynamics: Ionic Conductance, Osmotic Permeability, and the Electrostatic Potential Map. *Biophys. J.* **2005**, *88*, 3745−3761.
(4) Hub, J. S.; Aponte-Santamaría, C.; Grubmüller, H.; de Groot, B. L. Voltage-Regulated Water Flux through Aquaporin Channels in Silico. *Biophys. J.* **2010**, *99*, L97−L99.
(5) Jensen, M. Ø.; Jogini, V.; Borhani, D. W.; Leffler, A. E.; Dror, R. O.; Shaw, D. E. Mechanism of Voltage Gating in Potassium Channels. *Science* **2012**, *336*, 229−233.
(6) Vargas, E.; Yarov-Yarovoy, V.; Khalili-Araghi, F.; Catterall, W. A.; Klein, M. L.; Tarek, M.; Lindahl, E.; Schulten, K.; Perozo, E.; Bezanilla, F.; Roux, B. An Emerging Consensus on Voltage-Dependent Gating from Computational Modeling and Molecular Dynamics Simulations. *J. Gen. Physiol.* **2012**, *140*, 587−594.
(7) Tarek, M. Membrane Electroporation: A Molecular Dynamics Simulation. *Biophys. J.* **2005**, *88*, 4045−4053.
(8) Tieleman, D. P. The Molecular Basis of Electroporation. *BMC Biochem* **2004**, *5*, 10.
(9) Gurtovenko, A. A.; Vattulainen, I. Pore Formation Coupled to Ion Transport through Lipid Membranes as Induced by Transmembrane Ionic Charge Imbalance: Atomistic Molecular Dynamics Study. *J. Am. Chem. Soc.* **2005**, *127*, 17570−17571.
(10) BÖckmann, R. A.; De Groot, B. L.; Kakorin, S.; Neumann, E.; Grubmüller, H. Kinetics, Statistics, and Energetics of Lipid Membrane Electroporation Studied by Molecular Dynamics Simulations. *Biophys. J.* **2008**, *95*, 1837−1850.
(11) Ziegler, M. J.; Vernier, P. T. Interface Water Dynamics and Porating Electric Fields for Phospholipid Bilayers. *J. Phys. Chem. B* **2008**, *112*, 13588−13596.
(12) Delemotte, L.; Tarek, M. Molecular Dynamics Simulations of Lipid Membrane Electroporation. *J. Membr. Biol.* **2012**, *245*, 531−543.
(13) Abiror, I. G.; Arakelyan, V. B.; Chernomordik, L. V.; Chizmadzhev, Y. A.; Pastushenko, V.; Tarasevich, M. Electric Breakdown of Bilayer Lipid Membranes I. The Main Experimental Facts and Their Qualitative Discussion. *Bioelectrochem. Bioenerg.* **1979**, *6*, 37−51.
(14) Benz, R.; Beckers, F.; Zimmermann, U. Reversible Electrical Breakdown of Lipid Bilayer Membranes: A Charge-Pulse Relaxation Study. *J. Membr. Biol.* **1979**, *48*, 181−204.
(15) Kotnik, T.; Rems, L.; Tarek, M.; Miklavčič, D. Membrane Electroporation and Electropermeabilization: Mechanisms and Models. *Annu. Rev. Biophys.* **2019**, *48*, 63−91.
(16) Lambricht, L.; Lopes, A.; Kos, S.; Sersa, G.; Préat, V.; Vandermeulen, G. Clinical Potential of Electroporation for Gene Therapy and DNA Vaccine Delivery. *Expert Opinion on Drug Delivery* **2016**, *13*, 295−310.
(17) Aycock, K. N.; Davalos, R. V. Irreversible Electroporation: Background, Theory, and Review of Recent Developments in Clinical Oncology. *Bioelectricity* **2019**, *1*, 214−234.
(18) Geboers, B.; Scheffer, H. J.; Graybill, P. M.; Ruarus, A. H.; Nieuwenhuizen, S.; Puijk, R. S.; van den Tol, P. M.; Davalos, R. V.; Rubinsky, B.; de Gruijl, T. D.; Miklavčič, D.; Meijerink, M. R. High-Voltage Electrical Pulses in Oncology: Irreversible Electroporation, Electrochemotherapy, Gene Electrotransfer, Electrofusion, and Electroimmunotherapy. *Radiology* **2020**, *295*, 254−272.
(19) Zhong, Q.; Moore, P. B.; Newns, D. M.; Klein, M. L. Molecular Dynamics Study of the LS3 Voltage-Gated Ion Channel. *FEBS Lett.* **1998**, *427*, 267−270.
(20) Tieleman, D.; Berendsen, H.; Sansom, M. Voltage-Dependent Insertion of Alamethicin at Phospholipid/Water and Octane/Water Interfaces. *Biophys. J.* **2001**, *80*, 331−346.
(21) Roux, B. The Membrane Potential and Its Representation by a Constant Electric Field in Computer Simulations. *Biophys. J.* **2008**, *95*, 4205−4216.
(22) Gumbart, J.; Khalili-Araghi, F.; Sotomayor, M.; Roux, B. Constant Electric Field Simulations of the Membrane Potential Illustrated with Simple Systems. *Biochimica et Biophysica Acta (BBA) - Biomembranes* **2012**, *1818*, 294−302.
(23) Vernier, P. T.; Ziegler, M. J.; Sun, Y.; Gundersen, M. A.; Tieleman, D. P. Nanopore-Facilitated, Voltage-Driven Phosphatidylserine Translocation in Lipid Bilayers—in Cells and *in Silico*. *Phys. Biol.* **2006**, *3*, 233−247.
(24) Piggot, T. J.; Holdbrook, D. A.; Khalid, S. Electroporation of the E. Coli and S. Aureus Membranes: Molecular Dynamics Simulations of Complex Bacterial Membranes. *J. Phys. Chem. B* **2011**, *115*, 13381−13388.
(25) Fernández, M. L.; Marshall, G.; Sagués, F.; Reigada, R. Structural and Kinetic Molecular Dynamics Study of Electroporation in Cholesterol-Containing Bilayers. *J. Phys. Chem. B* **2010**, *114*, 6855−6865.
(26) Ho, M.-C.; Casciola, M.; Levine, Z. A.; Vernier, P. T. Molecular Dynamics Simulations of Ion Conductance in Field-Stabilized Nanoscale Lipid Electropores. *J. Phys. Chem. B* **2013**, *117*, 11633−11640.
(27) Sachs, J. N.; Crozier, P. S.; Woolf, T. B. Atomistic Simulations of Biologically Realistic Transmembrane Potential Gradients. *J. Chem. Phys.* **2004**, *121*, 10847−10851.
(28) Denning, E. J.; Crozier, P. S.; Sachs, J. N.; Woolf, T. B. From the Gating Charge Response to Pore Domain Movement: Initial Motions of Kv1.2 Dynamics under Physiological Voltage Changes. *Mol. Membr. Biol.* **2009**, *26*, 397−421.
(29) Kutzner, C.; Grubmüller, H.; De Groot, B. L.; Zachariae, U. Computational Electrophysiology: The Molecular Dynamics of Ion Channel Permeation and Selectivity in Atomistic Detail. *Biophys. J.* **2011**, *101*, 809−817.
(30) Ewald, P. P. The Calculation of Optical and Electrostatic Grid Potential. *Ann. Phys.* **1921**, *369*, 253−287.
(31) Darden, T.; York, D.; Pedersen, L. Particle Mesh Ewald: An N$ \cdot$log(N) Method for Ewald Sums in Large Systems. *J. Chem. Phys.* **1993**, *98*, 10089−10092.
(32) Essmann, U.; Perera, L.; Berkowitz, M. L.; Darden, T.; Lee, H.; Pedersen, L. G. A Smooth Particle Mesh Ewald Potential. *J. Chem. Phys.* **1995**, *103*, 8577−8592.
(33) Raiteri, P.; Kraus, P.; Gale, J. D. Molecular Dynamics Simulations of Liquid−Liquid Interfaces in an Electric Field: The Water−1,2-Dichloroethane Interface. *J. Chem. Phys.* **2020**, *153*, 164714.
(34) Gurtovenko, A. A.; Anwar, J.; Vattulainen, I. Defect-Mediated Trafficking across Cell Membranes: Insights from in Silico Modeling. *Chem. Rev.* **2010**, *110*, 6077−6103.
(35) Kopec, W.; Gapsys, V. Periodic Boundaries in Molecular Dynamics Simulations: Why Do We Need Salt? *bioRxiv*, 2022.
(36) Melcr, J.; Bonhenry, D.; Timr, Š.; Jungwirth, P. Transmembrane Potential Modeling: Comparison between Methods of Constant Electric Field and Ion Imbalance. *J. Chem. Theory Comput.* **2016**, *12*, 2418−2425.
(37) Hub, J. S. Joint Reaction Coordinate for Computing the Free-Energy Landscape of Pore Nucleation and Pore Expansion in Lipid Membranes. *J. Chem. Theory Comput.* **2021**, *17*, 1229−1239.
(38) Knight, C. J.; Hub, J. S. MemGen: A General Web Server for the Setup of Lipid Membrane Simulation Systems. *Bioinformatics* **2015**, *31*, 2897−2899.

(39) Berger, O.; Edholm, O.; Jähnig, F. Molecular Dynamics Simulations of a Fluid Bilayer of Dipalmitoylphosphatidylcholine at Full Hydration, Constant Pressure, and Constant Temperature. *Biophys. J.* **1997**, *72*, 2002−2013.
(40) Berendsen, H. J. C.; Postma, J. P. M.; DiNola, A.; Haak, J. R.; van Gunsteren, W. F. Molecular Dynamics with Coupling to an External Bath. *J. Chem. Phys.* **1984**, *81*, 3684−3690.
(41) Abraham, M. J.; Murtola, T.; Schulz, R.; Páll, S.; Smith, J. C.; Hess, B.; Lindahl, E. GROMACS: High Performance Molecular Simulations through Multi-Level Parallelism from Laptops to Supercomputers. *SoftwareX* **2015**, *1*, 19−25.
(42) Bussi, G.; Donadio, D.; Parrinello, M. Canonical Sampling through Velocity Rescaling. *J. Chem. Phys.* **2007**, *126*, 014101.
(43) Hub, J. S.; Awasthi, N. Probing a Continuous Polar Defect: A Reaction Coordinate for Pore Formation in Lipid Membranes. *J. Chem. Theory Comput.* **2017**, *13*, 2352−2366.
(44) Awasthi, N.; Hub, J. S. *Biomembrane Simulations. Computational Studies of Biological Membranes*; CRC Press, Taylor & Francis Group: 2019.
(45) Ting, C. L.; Awasthi, N.; Müller, M.; Hub, J. S. Metastable Prepores in Tension-Free Lipid Bilayers. *Phys. Rev. Lett.* **2018**, *120*, 128103.
(46) Verbeek, S. F.; Awasthi, N.; Teiwes, N. K.; Mey, I.; Hub, J. S.; Janshoff, A. How Arginine Derivatives Alter the Stability of Lipid Membranes: Dissecting the Roles of Side Chains, Backbone and Termini. *Eur. Biophys J.* **2021**, *50*, 127−142.
(47) Poojari, C. S.; Scherer, K. C.; Hub, J. S. Free Energies of Membrane Stalk Formation from a Lipidomics Perspective. *Nat. Commun.* **2021**, *12*, 6594.
(48) Hub, J. S.; de Groot, B. L.; van der Spoel, D. G_wham-A Free Weighted Histogram Analysis Implementation Including Robust Error and Autocorrelation Estimates. *J. Chem. Theory Comput.* **2010**, *6*, 3713−3720.
(49) Gunsteren, W. F. V.; Berendsen, H. J. C. *Gromos Manual*; BIOMOS, Biomolecular Software, Laboratory of Physical Chemistry, University of Groningen: 1987.
(50) Tieleman, D. P.; Leontiadou, H.; Mark, A. E.; Marrink, S.-J. Simulation of Pore Formation in Lipid Bilayers by Mechanical Stress and Electric Fields. *J. Am. Chem. Soc.* **2003**, *125*, 6382−6383.
(51) Tolpekina, T. V.; Den Otter, W. K.; Briels, W. J. Nucleation Free Energy of Pore Formation in an Amphiphilic Bilayer Studied by Molecular Dynamics Simulations. *J. Chem. Phys.* **2004**, *121*, 12060−12066.
(52) Bennett, W. D.; Sapay, N.; Tieleman, D. P. Atomistic Simulations of Pore Formation and Closure in Lipid Bilayers. *Biophys. J.* **2014**, *106*, 210−219.
(53) Awasthi, N.; Hub, J. S. Simulations of Pore Formation in Lipid Membranes: Reaction Coordinates, Convergence, Hysteresis, and Finite-Size Effects. *J. Chem. Theory Comput.* **2016**, *12*, 3261−3269.
(54) Hu, Y.; Sinha, S. K.; Patel, S. Investigating Hydrophilic Pores in Model Lipid Bilayers Using Molecular Simulations: Correlating Bilayer Properties with Pore-Formation Thermodynamics. *Langmuir* **2015**, *31*, 6615−6631.
(55) Weaver, J. C.; Chizmadzhev, Y. A. Theory of Electroporation: A Review. *Bioelectrochem. Bioenerg.* **1996**, *41*, 135−160.
(56) Kasparyan, G.; Hub, J. S. Molecular Simulations Reveal the Free Energy Landscape and Transition State of Membrane Electroporation. *bioRxiv*, 2023; DOI: 10.1101/2023.01.31.526495.
(57) de Leeuw, S.; Perram, J.; Smith, E. Simulation of Electrostatic Systems in Periodic Boundary Conditions. I. Lattice Sums and Dielectric Constants. *Proc. R. Soc. London A* **1980**, *373*, 27−56.
(58) Deserno, M.; Holm, C. How to Mesh up Ewald Sums. I. A Theoretical and Numerical Comparison of Various Particle Mesh Routines. *J. Chem. Phys.* **1998**, *109*, 7678.
(59) Hub, J. S.; de Groot, B. L.; Grubmüller, H.; Groenhof, G. Quantifying Artifacts in Ewald Simulations of Inhomogeneous Systems with a Net Charge. *J. Chem. Theory Comput.* **2014**, *10*, 381−390.
(60) Öhlknecht, C.; Lier, B.; Petrov, D.; Fuchs, J.; Oostenbrink, C. Correcting Electrostatic Artifacts Due to Net-charge Changes in the Calculation of Ligand Binding Free Energies. *J. Comput. Chem.* **2020**, *41*, 986−999.

https://doi.org/10.1021/acs.jctc.3c00065
J. Chem. Theory Comput. 2023, 19, 2676−2683